

# A Model for Multi-property Galaxy Cluster Statistics

August E. Evrard<sup>1,2,3</sup>, Pablo Arnault<sup>1,4</sup>, Dragan Huterer<sup>1</sup>, Arya Farahi<sup>1</sup>

<sup>1</sup>*Department of Physics and Michigan Center for Theoretical Physics, University of Michigan, Ann Arbor, MI 48109, USA.*

<sup>2</sup>*Department of Astronomy, University of Michigan, Ann Arbor, MI 48109, USA.*

<sup>3</sup>*Institut d’Astrophysique, 98bis Bd. Arago, 75012 Paris, France.*

<sup>4</sup>*École Normale Supérieure de Cachan, 61 Avenue du Président Wilson, 94230 Cachan, France.*

June 14, 2018

## ABSTRACT

The massive dark matter halos that host groups and clusters of galaxies have observable properties that appear to be log-normally distributed about power-law mean scaling relations in halo mass. Coupling this assumption with either quadratic or cubic approximations to the mass function in log space, we derive closed-form expressions for the space density of halos as a function of multiple observables as well as forms for the low-order moments of properties of observable-selected samples. Using a Tinker mass function in a  $\Lambda$ CDM cosmology, we show that the cubic analytic model reproduces results obtained from direct, numerical convolution at the 10% level or better over nearly the full range of observables covered by current observations and for redshifts extending to  $z = 1.5$ . The model provides an efficient framework for estimating effects arising from selection and covariance among observable properties in survey samples.

**Key words:** cosmology: clusters, cosmology: theory, galaxies: clusters: general: large-scale structure of universe

## 1 INTRODUCTION

Counts of galaxy clusters provide constraints on cosmological parameters (*e.g.*, Voit 2005; Allen, Evrard & Mantz 2011, and references therein), and test fundamental theories of gravity and cosmic acceleration (*e.g.*, Weinberg et al. 2013). Such studies typically use cluster samples identified via optical (Roza et al. 2010), X-ray (Mantz et al. 2010; Henry et al. 2009) or thermal Sunyaev-Zel’dovich (SZ, Benson et al. 2013; Sievers et al. 2013; Planck Collaboration et al. 2013) signatures of the baryons in the halos that host cluster phenomena. These analyses are empowered by simulation studies that calibrate the space density as a function of halo mass, known as the *mass function*, within a given cosmology (Tinker et al. 2008; Bhattacharya et al. 2011; Murray, Power & Robotham 2013).

Modeling the expected counts of clusters in a wide-area observational survey requires combining the mass function with a statistical model that expresses the likelihood for a halo of mass  $M$  at redshift  $z$  to have some intrinsic observable signal,  $S$ , detectable in the survey. Evidence from observations (Arnaud, Pointecouteau & Pratt 2005; Maughan 2007; Pratt et al. 2009; Vikhlinin et al. 2009; Zhang et al. 2011; Ruel et al. 2013; Saliwanchik et al. 2013; Ettori 2013; Maughan 2014) and simulations (Evrard et al. 2008; Stanek et al. 2010; Fabjan et al. 2011; Munari et al. 2013; Jiang

et al. 2013; Le Brun et al. 2013; Biffi et al. 2014) support a model in which the scaling law behavior is power-law with mass in the mean, with approximately log-normal variance.

While scaling behavior of cluster properties has been studied for decades (see Giodini et al. 2013, for a recent review), most works have focused on correlating pairs of observed signals,  $\{S_2, S_1\}$ , or on studying how a single observable scales with mass,  $\{S_1, M\}$ . Simulations provide a natural environment for the latter, since the true halo mass is known. For observations, mass estimates are made indirectly from measured signals, for example through assumption of virial or hydrostatic equilibrium, and this methodology introduces the potential for bias and additional variance that must be calibrated (*e.g.*, Rasia et al. 2012; Battaglia et al. 2013; Nelson et al. 2014). Alternatively, masses can be inferred through inversion of a given observable-mass relation. In this way, an observable serves as proxy for halo mass.

Evidence of biases in mass proxies can arise from comparisons among different observable signals. Planck satellite measurements of the thermal SZ effect in the optically-selected **maxBCG** sample (Planck Collaboration 2011) led to a detailed re-examination of X-ray, SZ and optical scaling relations by Roza et al. (2014a,b,c). That study concluded that the Planck  $Y_{SZ}$  mass calibration was biased low by a few tens of percent, a finding supported by independent

weak gravitational lensing estimates of Planck clusters (von der Linden et al. 2014), although other studies are less supportive (Israel et al. 2014).

Rozo et al. (2014b) present a model for multivariate signal counts and other statistics under the assumption of a locally power-law mass function. That model was employed to interpret a combined set of X-ray, SZ and optical data, resulting in a set of preferred scaling relations presented in Rozo et al. (2014c) (see their Table 4).

In this paper, we present a non-local extension of that model that expands its scope to effectively cover the complete dynamic range of properties displayed by the population of galaxy clusters. Within a  $\Lambda$ CDM cosmology, we show that the mass function of the massive halos that host groups and clusters of galaxies can be represented by a low-order polynomial (in log-space) to a typical accuracy of a few percent, comparable to its calibrated level of precision from N-body simulations. Convolving this mass function representation with a multivariate Gaussian of logarithmic halo properties at fixed mass and redshift results in analytic expressions for the space density as a function of multiple observables and other derivative statistics. By offering a fast method for estimating survey sample and follow-up study outcomes, this formalism is intended to complement data analysis methods based on similar model assumptions (Maughan 2014).

We employ a halo mass convention of  $M_{500c}$ , the mass within a spherical region encompassing 500 times the critical density,  $\rho_c(z)$ , but the analytic expressions can be applied using any choice of halo mass convention. We use  $M_{500c}$  to be consistent with the scaling laws presented in Rozo et al. (2014c). In §2, we derive expressions for multi-observable cluster population statistics using low-order polynomial approximations of the mass function in log space. These are then applied to X-ray and SZ statistics in §3. In §4, we discuss some of the model’s strengths and limitations, and we summarize our results in §5

## 2 MODEL FOR LOW-ORDER MOMENTS

We first develop expressions for the space density of clusters as a function of observables such as temperature or luminosity, then compute first and second moments for properties of samples selected by a specific observable. Our model expands the results presented in Rozo et al. (2014b) and uses slightly different notation.

Consider a set of  $N$  bulk observable properties  $S_a$  where  $a \in \{1, N\}$ ; these observables can be, for example, X-ray luminosity,  $L_X$ , temperature,  $T_X$ , gas thermal energy measured in the X-ray or SZ flux,  $Y_X$  or  $Y_{SZ}$ , number of galaxies,  $N_{\text{gal}}$  or  $\lambda$ , inferred lensing mass  $M_{\text{lens}}$ , etc. measured within some characteristic radius. Let  $s_a \equiv \ln(S_a)$  represent the natural logarithms of these properties in some chosen basis of units (for example,  $10^{44}$  erg s $^{-1}$  for X-ray luminosity).

We assume power-law forms for the observable–mass scaling relations. Choosing a halo pivot mass scale,  $M_p$ , at some fiducial redshift (values discussed below), and letting  $\mu \equiv \ln(M/M_p)$ , the vector of log-observables,  $\mathbf{s}$ , scales in the

mean with mass as

$$\langle \mathbf{s} | \mu \rangle = \boldsymbol{\pi} + \boldsymbol{\alpha} \mu, \quad (1)$$

where the vectors  $\boldsymbol{\pi}$  and  $\boldsymbol{\alpha}$  are the normalizations and slopes of the relevant scaling laws. We consider redshift-dependent normalizations,  $\boldsymbol{\pi}(z)$ , that scale in a self-similar manner (Böhlinger, Dolag & Chon 2012). While the slopes may also be redshift-dependent, we take them as constant here.

Individual halos drawn from the cosmic population deviate from this mean behavior in a manner that we assume is log-normal. At all redshifts, the full probability density function,  $P(\mathbf{s} | \mu)$ , is described by a covariance matrix with elements  $C_{ab} = \langle (s_a - \langle s_a | \mu \rangle)(s_b - \langle s_b | \mu \rangle) \rangle$ , and where  $C_{aa} = \sigma_a^2$  is the intrinsic log variance of the  $a^{\text{th}}$  observable. We assume this covariance to be independent of mass and redshift.

### 2.1 First-order (local) mass function

The model of Rozo et al. (2014b) uses a first-order Taylor expansion of the mass function,  $n(\ln M)$  (with dimension of number density per  $\ln(M)$ ), around some pivot mass  $M_p$ ,

$$n_1(\mu) = A e^{-\beta_1 \mu}, \quad (2)$$

where  $A$  and  $\beta_1$  are the local amplitude and (negative) slope of the mass function evaluated at the pivot,  $\mu = 0$ . Note that  $A$  and  $\beta_1$  are functions of redshift, cosmology, and pivot location, as explained in §3 below. The subscript on the space density indicates the first-order nature of the mass function expansion.

Using equations (2) and (1), Bayes theorem in the form  $P(\mu | \mathbf{s}) = P(\mathbf{s} | \mu)P(\mu)/P(\mathbf{s})$  allows us obtain the mean and variance of the log mass selected by a fixed combination of observables. In the first-order approximation to the mass function, this probability is Gaussian, with mean and variance

$$\langle \mu | \mathbf{s} \rangle_1 = \left[ \boldsymbol{\alpha}^T \mathbf{C}^{-1} (\mathbf{s} - \boldsymbol{\pi}) - \beta_1 \right] \sigma_{\mu | \mathbf{s}, 1}^2, \quad (3)$$

$$\sigma_{\mu | \mathbf{s}, 1}^2 = (\boldsymbol{\alpha}^T \mathbf{C}^{-1} \boldsymbol{\alpha})^{-1}. \quad (4)$$

In the case of a single observable quantity  $s_a$ , these expressions reduce to  $\langle \mu | s_a \rangle_1 = (s_a - \pi_a) / \alpha_a - \beta_1 \sigma_{\mu | a, 1}^2$  and  $\sigma_{\mu | a, 1}^2 = (\sigma_a / \alpha_a)^2$ . The mean mass is biased low relative to the assumed scaling by an amount given by the product of the local slope of the mass function and the mass variance of the chosen observable.

**Space density of multiple observables.** Convolving equation (2) with the log-normal likelihood,  $P(\mathbf{s} | \mu)$ , yields the halo number density as a function of the full vector of observable properties,

$$n_1(\mathbf{s}) = A'_1 \exp \left[ -\frac{1}{2} \left( (\mathbf{s} - \boldsymbol{\pi})^T \mathbf{C}^{-1} (\mathbf{s} - \boldsymbol{\pi}) - \frac{\langle \mu | \mathbf{s} \rangle_1^2}{\sigma_{\mu | \mathbf{s}, 1}^2} \right) \right],$$

$$A'_1 = A \sigma_{\mu | \mathbf{s}, 1} \left( (2\pi)^{N-1} |\mathbf{C}| \right)^{-1/2}. \quad (5)$$

**Observable-selected samples.** Now consider selecting a sample by a certain observable,  $s_a$ . With the full space density above, we can derive the probability density function (PDF) of any second observable,  $s_b$ , by  $P(s_b | s_a) =$

$n(s_a, s_b)/n(s_a)$ . The result is also Gaussian with mean and variance

$$\langle s_b | s_a \rangle_1 = \pi_b + \alpha_b [\langle \mu | s_a \rangle_1 + \beta_1 r_{ab} \sigma_{\mu|a,1} \sigma_{\mu|b,1}], \quad (6)$$

$$\sigma_{b|a,1}^2 = \alpha_b^2 [\sigma_{\mu|a,1}^2 + \sigma_{\mu|b,1}^2 - 2r_{ab} \sigma_{\mu|a,1} \sigma_{\mu|b,1}], \quad (7)$$

where  $r_{ab}$  is the correlation coefficient between properties  $s_a$  and  $s_b$  at fixed mass. When the intrinsic correlation of these observables is non-zero, then a shift in the mean of  $s_b$  is induced that is similar in form to the bias of equation (3) but with opposite sign if  $r_{ab}$  is positive. This effect can be understood by the fact that the dominant lower mass halos that scatter upward into the chosen  $s_a$  bin will also have a positive deviation from the mean  $s_b$  if  $r_{ab}$  is positive. If  $r_{ab}$  is negative, the effect is reversed.

Along with these purely observable properties, one can compute the correlation coefficient between mass and  $s_b$  for samples chosen by  $s_a$ , finding

$$r_{(\mu b|a),1} = \frac{\sigma_{\mu|a,1}/\sigma_{\mu|b,1} - r_{ab}}{[1 - r_{ab}^2 + (\sigma_{\mu|a,1}/\sigma_{\mu|b,1} - r_{ab})^2]^{1/2}}. \quad (8)$$

In the case of uncorrelated observables ( $r_{ab} = 0$ ), a positive correlation between mass and  $s_b$  is induced by the fact that halos with lower mass that scattered up into the  $s_a$  bin will also have lower  $s_b$ , and vice-versa. In the limit that the selection property,  $s_a$ , is a much better mass proxy than  $s_b$ , such that  $\sigma_{\mu|a,1}/\sigma_{\mu|b,1} \simeq 0$ , then the correlation of  $s_b$  and mass takes on the opposite sign of the intrinsic correlation,  $r_{ab}$ . Relative to the mean behavior in the selection bin, halos with of lower mass,  $\Delta\mu < 0$ , will have positively enhanced selection signal at that mass,  $\Delta s_a > 0$ , and then  $\Delta s_b \simeq r_{ab} \Delta s_a \simeq -r_{ab} \Delta\mu$ .

## 2.2 Higher-order (non-local) mass functions

The first-order model functions well over a relatively narrow range in mass or observable near the chosen pivot point. We now wish to extend the range of the model by introducing quadratic and cubic terms into the mass function approximation. We derive here exact expressions for the quadratic case, and approximate expressions for the cubic case, and show below that the latter are accurate to better than 10% for a wide range of halo mass scales and redshifts.

The second-order model uses a mass function,

$$n_2(\mu) = A e^{-\beta_1 \mu - \frac{1}{2} \beta_2 \mu^2}, \quad (9)$$

where  $\beta_2$  is the magnitude of the second derivative of the mass function at the pivot mass scale, which is negative for massive halos in  $\Lambda$ CDM cosmologies.

The convolution remains analytic, and the halo number density as a function of multiple observables retains the form of equation (5), but adding local curvature reduces the weight of lower-mass halos scattered upward into the signal bin. Consequently, the gaussian distribution of halo mass at fixed observable properties has a compressed mean and variance relative to the first-order treatment,

$$\langle \mu | \mathbf{s} \rangle_2 = x_{\mathbf{s}} \langle \mu | \mathbf{s} \rangle_1, \quad (10)$$

$$\sigma_{\mu|\mathbf{s},2}^2 = x_{\mathbf{s}} \sigma_{\mu|\mathbf{s},1}^2, \quad (11)$$

where the compression factor,  $x_{\mathbf{s}} \equiv (1 + \beta_2 \sigma_{\mu|\mathbf{s},1}^2)^{-1}$ , is less than unity and is well approximated by  $1 - \beta_2 \sigma_{\mu|\mathbf{s},1}^2$  for most of the applications discussed below.

Consider again the case of two observables  $s_a$  and  $s_b$ . The PDF of having observable  $s_b$  in a population selected by observable  $s_a$  also remains Gaussian, and the expressions written in mass equivalents are somewhat simpler. Letting  $\delta_i = (s_i - \pi_i)/\alpha_i$ , then the mean and variance for the second-order mass function approximation are

$$\langle \delta_b | s_a \rangle_2 = x_a [\langle \mu | s_a \rangle_1 + (\beta_1 + \beta_2 \delta_a) r_{ab} \sigma_{\mu|a,1} \sigma_{\mu|b,1}], \quad (12)$$

$$\frac{\sigma_{b|a,2}^2}{\alpha_b^2} = x_a \left[ \frac{\sigma_{b|a,1}^2}{\alpha_b^2} + \beta_2 \sigma_{\mu|a,1}^2 \sigma_{\mu|b,1}^2 (1 - r_{ab}^2) \right]. \quad (13)$$

The first expression indicates that the mean observable now senses the curvature in the mass function through the  $\beta_2 \delta_a$  term, where recall that  $\delta_a$  is measuring the equivalent log-mass distance from the pivot location.

In the limit of uncorrelated observables ( $r_{ab} = 0$ ), the second expression reduces to  $x_a \sigma_{\mu|a,1}^2 + \sigma_{\mu|b,1}^2$ , as it should since the mass function curvature affects the mass variance in the selection variable but not that of the non-selection variable.

Finally, the correlation coefficient between mass and property  $s_b$  at fixed  $s_a$  is now given by

$$r_{(\mu b|a),2} = \frac{\sigma_{\mu|a,1}/\sigma_{\mu|b,1} - r_{ab}}{[(1 - r_{ab}^2)/x_a + (\sigma_{\mu|a,1}/\sigma_{\mu|b,1} - r_{ab})^2]^{1/2}}. \quad (14)$$

For uncorrelated observables this expression again reduces to equation (8) with  $\sigma_{\mu|a,2}^2$  replacing  $\sigma_{\mu|a,1}^2$ .

In the Appendix, we show a further extension to the third-order, with  $n_3(\mu) = A e^{-\beta_1 \mu - \frac{1}{2} \beta_2 \mu^2 - \frac{1}{6} \beta_3 \mu^3}$ .

## 3 APPLICATIONS TO OBSERVABLE CLUSTER PROPERTIES

We now evaluate the utility of the above expressions by comparing their predictions to expectations calculated via explicit local convolution of the Tinker mass function (Tinker et al. 2008). For hot gas observables, we examine the X-ray luminosity at soft photon energies,  $L_X$  and the total gas thermal energy as determined by the thermal SZ,  $Y_{SZ}$ . These cases represent examples of relatively high and low-scatter mass proxies, respectively. We also examine the case optical richness,  $N_{\text{gal}}$ , a relatively high-scatter proxy for which the correlation with hot gas properties at fixed mass is currently poorly understood.

We perform analysis at  $z = 0.23$ , the redshift where local mass-observable relations used here are calibrated, and also at  $z = 1.5$ . The higher redshift is chosen to be representative of the outer reaches of near-term cluster surveys and is also an epoch at which the mass function is both steeper and more strongly curved compared to low redshift, aspects that make the higher-order corrections more important.

### 3.1 Mass function and log-space polynomial fits

The Tinker mass function employs an updated version of the normalized mass fraction functional,  $f(\sigma)$ , in the form

**Table 1.** Mass function expansion parameters at two redshifts for a WMAP7 cosmology. The pivot mass,  $M_p$ , is in units of  $10^{14} M_\odot$  and the amplitude,  $A$ , is in units of  $10^{-6} \text{Mpc}^{-3}$ .

$z$	$M_p$	$A$	$\beta_1$	$\beta_2$	$\beta_3$
0.23	2.0	1.944	1.97	0.70	0.40
1.5	1.0	0.293	3.07	1.20	0.73

originally calibrated for CDM cosmologies by Sheth, Mo & Tormen (2001) and Jenkins et al. (2001),

$$n_{\text{Tinker}}(\mu, z) = \frac{dn}{d\mu} = \frac{\bar{\rho}_m(z)}{M} \frac{d \ln \sigma^{-1}(M, z)}{d\mu} f(\sigma), \quad (15)$$

where  $\bar{\rho}_m(z)$  is the mean cosmic matter density, and  $\sigma^2(M, z)$  is the linearly evolved variance of matter density fluctuations filtered on a mass scale  $M \equiv M_p e^\mu$ , both evaluated at redshift  $z$ . In this work, we use the mass function calculator published by Murray, Power & Robotham (2013) and employ the Tinker fit for  $f(\sigma)$  (Tinker et al. 2008) using the CAMB transfer function of a WMAP7 cosmology. The cosmological parameters for the  $\Lambda$ CDM model are: scaled Hubble constant,  $h = 0.704$ , baryon, cold dark matter and dark energy parameters of,  $\Omega_b = 0.0455$ ,  $\Omega_c = 0.226$ ,  $\Omega_{\text{DE}} = 0.728$ , respectively, spectral index,  $n_s = 0.967$ , and present amplitude of matter density fluctuations,  $\sigma_8 = 0.81$ .

At our two fiducial redshifts, we compute the coefficients  $A$ ,  $\beta_1$ ,  $\beta_2$  and  $\beta_3$  by taking numerical derivatives of  $n_{\text{Tinker}}(\mu, z)$  at the chosen pivot mass. Values of the pivot mass,  $M_p$ , in units of  $10^{14} M_\odot$  along with the fit parameters are shown in Table 1. At higher redshifts, the mass function steepens and becomes more strongly curved. For observables with large mass variance the second-order compression factor,  $1 + \beta_2 \sigma_{\mu|s}^2$  can be important since  $\beta_2 = 0.70$  and  $1.22$  at redshifts  $z = 0.23$  and  $1.5$ , respectively.

### 3.2 Scalings for $L_X$ , $Y_{SZ}$ , and $N_{\text{gal}}$

As specific examples of scaling laws we use results derived in the pan-chromatic study of Rozo et al. (2014c). In that work,  $L_X$  is the X-ray luminosity in the rest-frame  $[0.1, 2.4]$  keV band, expressed in units of  $10^{44}$  ergs/s and measured within a cylindrical aperture of radius  $R_{500c}$ . The thermal SZ signal,  $D_A^2 Y_{SZ}$  where  $D_A$  is the angular distance of the source, is given in units of  $10^{-5} \text{Mpc}^2$  and is measured within the spherical aperture of radius  $R_{500c}$ . The optical richness,  $N_{\text{gal}}$ , is the count of red sequence galaxies determined by the maxBCG cluster-finding algorithm within an estimated sphere of radius  $R_{200c}$  (Koester et al. 2007).

We use the observable—mass parameters,  $\pi_s$ ,  $\alpha_s$ , and  $\sigma_{\ln S}$ , at  $z = 0.23$  given in Table 4 of Rozo et al. (2014c). The parameters, with normalizations rescaled to our choice of pivot mass,  $2 \times 10^{14} M_\odot$ , are summarized in Table 2. At  $z = 1.5$ , we employ self-similar scalings for normalizations of  $L_X$  and  $Y_{SZ}$  discussed below.

For the optical richness, we use a simple inversion of the scaling of lensing mass at fixed  $N_{\text{gal}}$  and consider both the published value of the scatter as well as a more optimistic value that is appropriate for the multi-color richness estimator,  $\lambda$  (Rykoff et al. 2012; Rozo & Rykoff 2013). The

**Table 2.** Observable-mass scaling parameters at  $z = 0.23$  and pivot mass,  $M_p = 2 \times 10^{14} M_\odot$ , from Rozo et al. (2014c). See text for unit definitions. Along with the published scatter values for  $N_{\text{gal}}$ , we also consider a smaller value in parentheses based on the  $\lambda$  richness estimator (Rykoff et al. 2012).

$S$	$S_p = e^{\pi_s}$	$\alpha_s$	$\sigma_{\ln S}$	$\sigma_{\mu s}$
$L_X$	0.61	1.55	0.39	0.252
$D_A^2 Y_{SZ}$	0.62	1.71	0.15	0.088
$N_{\text{gal}}$	37	0.94	0.42 (0.21)	0.45 (0.23)

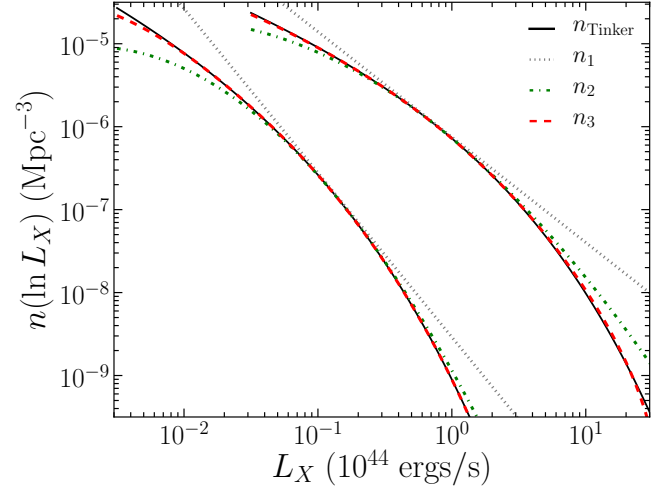


**Figure 1.** Comoving space density of halos as a function of  $L_X$  evaluated at redshift  $z = 0.23$  (upper curves) and  $z = 1.5$  (lower), assuming self-similar redshift evolution of the X-ray normalization for the latter. Black lines show expectations from local convolution of the Tinker mass function, while the dotted (grey), dot-dashed (green) and dashed (red) curves show our analytic expressions based on first, second and third-order mass function expansions, respectively. Pivot masses of  $M_p = 2$  and  $1 \times 10^{14} M_\odot$  are used at  $z = 0.23$  and  $1.5$ , respectively, and the latter are offset by a factor of 0.1 in  $L_X$  for clarity. Deviations of the approximations from the direct Tinker convolution are plotted in Figure 2.

improvement of a factor of four in variance has significant implications that we illustrate below.

### 3.3 Application to cluster number counts

We first compare the approximate analytical formulae,  $n_i(\ln S)$ , to  $n_{\text{Tinker}}(\ln S)$ , where the latter quantity is obtained by explicit convolution of the Tinker mass function,  $\int n_{\text{Tinker}}(\mu) P(\ln S|\mu) d\mu$ .

In Figure 1 we show the X-ray luminosity function at redshifts  $z = 0.23$  and  $z = 1.5$ , derived using the parameters in Tables 1 and 2. The normalization of the high redshift  $L_X$ — $M$  relation is scaled using the assumption that the soft-band luminosity at fixed mass scale in a self-similar fashion,  $L(z) \sim H(z)^2$  (Böhringer, Dolag & Chon 2012). While the first-order model is locally accurate, the second- and third-order models extend the accuracy over increasingly wider ranges X-ray luminosity. The third-order model traces well

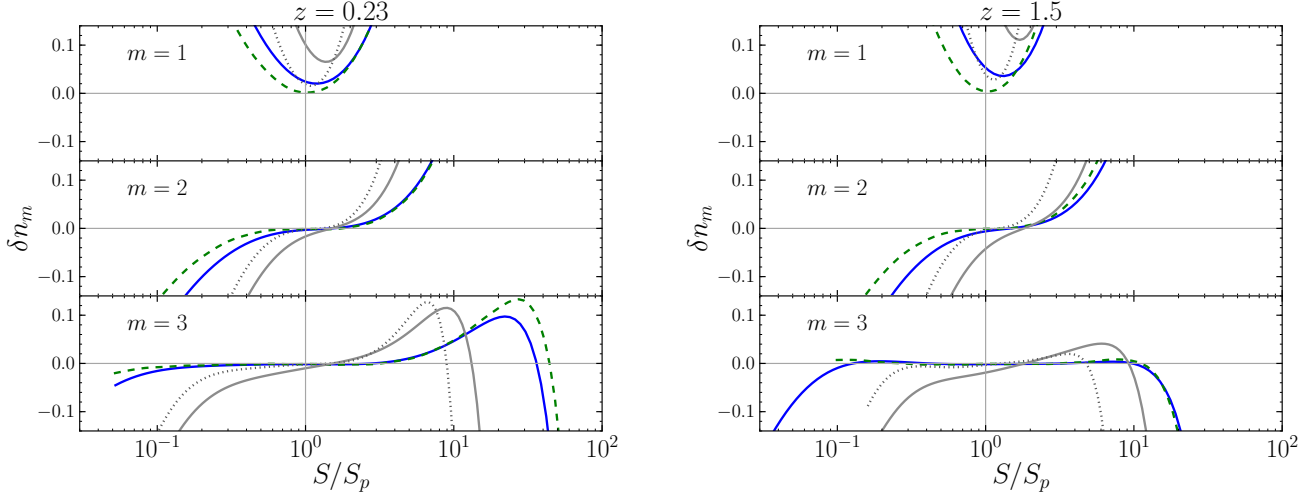


**Figure 2.** Fractional error in number counts,  $\delta n_m(\ln S) \equiv n_m(\ln S)/n_{\text{Tinker}}(\ln S) - 1$ , are shown for first, second, and third-order expansions of the log-space mass function (top to bottom) at  $z = 0.23$  (left) and  $1.5$  (right). The observable signals  $S$  represented are X-ray luminosity,  $L_X$  (blue solid lines), the SZ flux,  $D_A^2 Y_{SZ}$  (green dashed) and the optical richness,  $N_{\text{gal}}$ , using either the high scatter value,  $\sigma_\mu = 0.45$  (grey solid) or low value,  $\sigma_\mu = 0.23$  (grey dotted). Signals are plotted relative to the log-mean values,  $S_p$ , expected at the pivot mass scales of 2 and  $1 \times 10^{14} M_\odot$  (left and right, respectively) using parameters in Table 2.

the local Tinker convolution results across more than two decades in luminosity.

In Figure 2, we evaluate the accuracy of the different orders for all observables listed in Table 2. Values of the properties range from 0.03 – 100 for  $L_X/10^{44}$  erg s $^{-1}$  and  $D_A^2 Y_{SZ}/10^{-5}$  Mpc $^2$  and 3 – 1000 for  $N_{\text{gal}}$ .

At first order, the first-order counts always overestimate the Tinker convolved estimates. The normalization error is approximately  $1 - \sqrt{x_s} \simeq \beta_2 \sigma_{\mu|a,1}^2 / 2$ . The first-order approximation is thus most accurate for  $Y_{SZ}$  at low redshift and worst for  $N_{\text{gal}}$  at high redshift. With  $x_s = 0.80$ , the first-order  $N_{\text{gal}}$  counts at  $z = 1.5$  lie more than 10% above the Tinker convolution, even near the pivot point. When the optical richness scatter is reduced by a factor of two (dotted grey lines), the first-order improve dramatically. In all cases, the range within which the first-order estimates are accurate is limited to a factor of a few close to the pivot location.

At second order, the dynamic range over which the counts lie within 5% of the Tinker expectations widens, reaching nearly a decade for  $Y_{SZ}$  and  $L_X$  at low redshift. The approximation is always better at low redshifts where the second and third derivatives,  $\beta_2$  and  $\beta_3$ , of the mass function are lower. Note that the zero crossing is shifted upward from the pivot location by an amount that scales with the signal variance.

The third-order approximation is accurate to within 5% in number over more than two decades in both  $L_X$  and  $Y_{SZ}$ , with the larger errors only occurring at high signal values that correspond to  $M_{500}$  masses above 1 and  $0.5 \times 10^{15} M_\odot$  at low and high redshift, respectively. Such massive halos are quite rare, with space densities of roughly 20 and 0.2 per cubic gigaparsec at  $z = 0.23$  and 1.5. For statistical cluster samples that typically reach space densities many times higher, the third-order model is capable of yielding

highly accurate estimates of counts as a function of observable properties.

One can always vary the pivot mass scale in order to improve the quality fit over a certain range of signal. However, even with a tuned pivot, the first and second-order models cannot reach 10% accuracy over the wide dynamic range of observables covered by current surveys. In particular, unless the pivot mass scale is chose to be very high, it is very difficult for these models to obtain good accuracy at large masses and high redshifts.

### 3.4 Observable-selected sample expectations

Dedicated follow-up observations or joint studies of overlapping surveys at different wavelengths can allow multiple properties to be measured for clusters selected by a particular observable. Here, we explore expectations for such secondary properties based on the different orders of the multivariate model of §2.

Figure 3 shows an example for low redshift ( $z = 0.23$ ) in the form of the SZ thermal decrement expected for clusters selected at fixed X-ray luminosity. We chose a relatively bright luminosity of  $L_X = 10^{45}$  ergs/s appropriate for a mass scale of  $1.2 \times 10^{15} M_\odot$ , a factor of six above the low redshift pivot point. The correlation coefficient,  $r$ , between  $\ln(D_A^2 Y_{SZ})$  and  $\ln(L_X)$  is expected to be positive since both signals scale as positive powers of the intracluster gas mass and temperature (Stanek et al. 2010; Angulo et al. 2012). We take  $r = 0.5$  as an example value.

In Figure 3, the first order likelihood overestimates the mean by  $\sim 20\%$ . This relatively small error arises from near-cancellation of the much larger errors made in both  $n_1(\ln L_X, \ln D_A^2 Y_{SZ})$  and  $n_1(\ln L_X)$  relative to their Tinker values at this high mass. The first-order model is surprisingly accurate for conditional likelihoods.

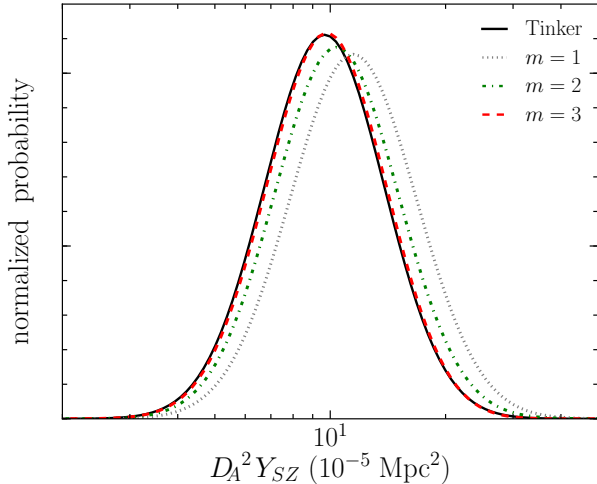


**Figure 3.** Probability density function,  $P(\ln S_b|S_a)$ , for the SZ signal,  $S_b = D_A^2 Y_{SZ}$ , at a chosen X-ray luminosity,  $S_a = L_X = 10^{45}$  ergs/s at  $z = 0.23$  as inferred from direct convolution of the Tinker mass function (black line) or from the approximate model using first (grey, dotted), second (green, dot-dashed) and third-order (red, dashed) forms.

By sensing the local mass function curvature, the second-order estimate, equation (12), corrects the first-order logarithmic mean by roughly  $\alpha_b(x_a - 1) \simeq -0.07$ , which reduces, but does not fully eliminate, the discrepancy with the local Tinker convolution. The third-order succeeds in matching the local Tinker probability with high accuracy.

The behavior of the low-order analytical likelihoods depends primarily on the mass variance of the selection variable and the signal value relative to the pivot location. Choosing  $Y_{SZ}$  as the selection variable yields a compression factor,  $x_s$ , of 0.995, much closer to unity than the 0.957 value for  $L_X$ , and thus the errors at all orders are considerably reduced.

Keeping  $L_X$  as the selection variable but selecting at an X-ray luminosity *below*, rather than above, the pivot luminosity,  $L_p$  results in different behavior because the corrections at odd and even orders have different signs. Selecting at  $L_X = L_p/A$ , where  $A > 1$ , the first-order mean  $\ln D_A^2 Y_{SZ}$  lies lower than the Tinker expectation, but the overshoot is smaller in magnitude than for the case of selecting at  $L_X = AL_p$ . The second-order correction then slightly overcorrects, with the mean *above* the Tinker estimate. The third-order applies a small, negative correction to closely align with the Tinker value.

### 3.5 Covariance between high-scatter mass proxies

As a final demonstration of the model, we examine effects of covariance between  $N_{\text{gal}}$  and  $L_X$ , the relatively poor mass proxies used here with  $\ln M$  scatter of 0.45 and 0.25, respectively (see Table 2). There are currently no theoretical or empirical constraints on the covariance between cold and hot baryons at fixed halo mass and redshift, so there is complete freedom in choosing the correlation coefficient,  $r$ , linking their deviations about the mean scaling behavior.

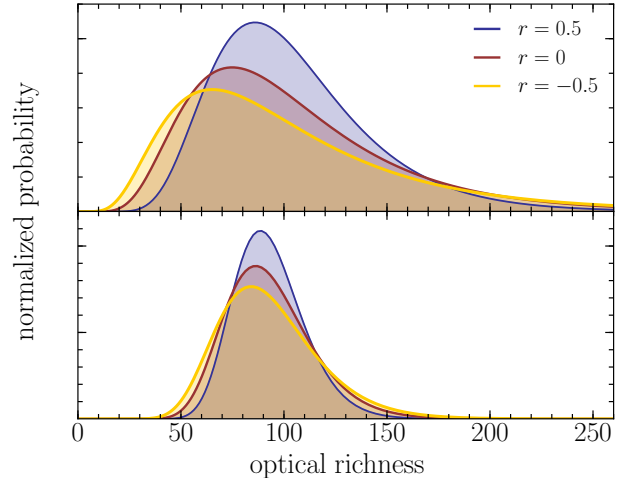


**Figure 4.** Expectations for optical richness at  $z = 0.23$  are demonstrated for two extreme cases. The top panel selects halos with  $L_X = 2.5 \times 10^{44}$  erg s $^{-1}$  and assumes a log-mass scatter at fixed richness of 0.45, appropriate for the original maxBCG sample  $N_{\text{gal}}$  richness estimator. The lower panel selects halos with  $D_A^2 Y_{SZ} = 3 \times 10^{-5}$  Mpc $^2$  and assumes a log-mass scatter at fixed richness of 0.23, appropriate for the improved  $\lambda$  richness estimator. In both panels, the different PDF's arise from different choices of correlation coefficient between richness and the selection variable, as indicated by the legend. The third-order, log-space approximation to the mass function is used in all calculations.

We then contrast the outcome of this case against an example using the improved richness estimator,  $\lambda$ , assumed to have mass scatter of 0.23, for halos selected using the superior mass proxy,  $Y_{SZ}$ , with mass scatter of 0.088.

From equation (12), with the aforementioned values for the mass scatter for the two proxies, the shift in mean expected in  $N_{\text{gal}}$  at fixed  $L_X$  as  $r$  is varied from  $-0.5$  to  $0.5$  will be of order 0.11 times the magnitude of the local logarithmic slope of the mass function. At a mass scale of  $5 \times 10^{14} M_{\odot}$ , the latter is of order three, implying a shift of roughly 30%. In addition, the variance, equations (7) and (13), is maximized when the properties strongly anti-correlate while it is minimized as  $r \rightarrow 1$ .

In the top panel of Figure 4, we show the likelihood of optical richness at  $z = 0.23$  for halos selected to have an X-ray luminosity of  $2.5 \times 10^{44}$  erg s $^{-1}$ , which highlights a mass  $M_{500} \simeq 5 \times 10^{14} M_{\odot}$ . The third-order estimator is used to calculate the conditional likelihood, and we show expectations for three discrete values of the correlation coefficient,  $r = -0.5, 0, 0.5$ .

As anticipated, the large mass scatter in these proxies means that predictions for the mean and variance in  $N_{\text{gal}}$  shift considerably as  $r$  is varied. The modal value of  $N_{\text{gal}}$  is 62 for  $r = -0.5$ , increasing to 86 at  $r = 0.5$ , while the scatter in  $\ln N_{\text{gal}}$  drops from 0.60 to 0.38 for these two cases. These effects conspire to dramatically change the  $2.5\sigma$  lower limits for  $N_{\text{gal}}$ , with values of 14 and 33 for  $r = -0.5$  and  $0.5$ , respectively.

Observational data demonstrate a large scatter between the richness,  $N_{\text{gal}}$ , and X-ray luminosity (*e.g.*, Rykoff et al.

2008; Andreon & Hurn 2010), but a new approach to estimating optical richness from multi-color photometry offers significant improvement. The  $\lambda$  richness estimator (Rykoff et al. 2012) uses a probabilistic membership trained on spectroscopic calibration of the red sequence in multi-color space. This richness estimator shows considerably smaller scatter in  $L_X$  compared to  $N_{\text{gal}}$  and the technique has been extended for use as a cluster finder in photometric surveys (Rykoff et al. 2013). Based on matching clusters found in the SDSS DR-8 sample to known X-ray clusters, Rozo & Rykoff (2013) demonstrate that the implied mass scatter of the  $\lambda$  richness measure is  $\sim 25\%$ , considerably reduced relative to the original  $N_{\text{gal}}$  richness.

The lower panel of of Figure 4 demonstrates how the use of low scatter mass proxies can significantly tighten the conditional likelihood of optical richness. Shown is the likelihood,  $p(\lambda|Y_{SZ})$  at  $z = 0.23$  for  $D_A^2 Y_{SZ} = 3 \times 10^{-5} \text{Mpc}^2$ , a value that selects roughly the same mass as the  $L_X$  choice used in the top panel. We assume 23% mass scatter in  $\lambda$  and 8.8% mass scatter in  $Y_{SZ}$ . Relative to the top panel, the scatter in  $P(\lambda|Y_{SZ})$  is reduced by more than a factor of two, and the sensitivity of  $\langle \lambda|Y_{SZ} \rangle$  to the correlation coefficient is also weakened.

## 4 DISCUSSION

We have emphasized an application of the model to the massive halos that host galaxy clusters at late cosmic times, but the mathematical framework is general, so the model could be applied at earlier epochs to describe phenomenology associated with the high-mass end of the mass function. Galaxies and quasars at redshifts of a few or early star formation at redshifts of tens are potential applications. The key requirements are observables or properties that of halos that scale as power-laws with halo mass in the mean, with variability described by a log-normal covariance.

Applied to groups and clusters, the third-order model is essentially global in scope. Compared to local Tinker convolution estimates, the cubic approximation achieves better than 10% accuracy over nearly the whole signal ranges covered by current observations, and for redshifts  $z < 1.5$ . This level of accuracy is comparable to the current level of systematic uncertainty in the mass function derived from simulations, particularly when the effects of baryon physics are included (Stanek, Rudd & Evrard 2009; Martizzi et al. 2013; Cusworth et al. 2013; Cui, Borgani & Murante 2014).

The pivot location sets the range of accuracy for the lower-order approximations. Since the third-order approximation is based on a Taylor expansion of  $e^{-\beta_3 \mu^3/6} \simeq 1 - \beta_3 \mu^3/6$ , where  $\mu = \ln(M/M_p)$ , the model breaks down as  $\mu^3 \rightarrow 6/\beta_3$ . For the pivots chosen here, this occurs only for very rare, massive systems with  $M_{500} \gtrsim 10^{15} M_\odot$ . To achieve the widest possible dynamic range, the second-order expressions could be interpolated using multiple pivot points,  $M_{p,k}$ , requiring values of  $\beta_1(M_{p,k}, z)$  and  $\beta_2(M_{p,k}, z)$  to be provided. For light-cone applications, these derivatives could be modeled as low-order polynomials in redshift.

The pivot masses we employ at the two demonstra-

tion redshifts correspond closely to those satisfying a fixed sky surface density condition,  $dN(> M)/dz = \text{const.}$ , in a  $\Lambda$ CDM cosmology (Evrard et al. 2002; Mortonson, Hu & Huterer 2011). For cluster survey applications, this would seem a natural choice.

While power-law scaling with log-normal covariance is supported for intrinsic properties of clusters, the available evidence is often limited. In particular, covariance among different signals is poorly understood (Maughan 2014) and there are few constraints as to whether the slope and variance of a particular signal's scaling with mass is indeed constant with mass and redshift, as is assumed here (*e.g.*, Balaguera-Antolínez et al. 2012, provide a hint of evidence for curvature in the  $L_X$ - $M$  relation). Redshift dependencies are easily incorporated into the existing framework by writing the slopes,  $\alpha(z)$ , intercepts,  $\pi(z)$ , and covariance,  $C(z)$ , as explicit functions of  $z$ . Extensions to the model that incorporate weak mass dependence in the scaling parameters are also possible.

The model covariance can be interpreted as that among intrinsic properties of halos, but signals observed from real clusters inevitably include projection effects and noise, including potential bias, associated with signal detection and characterization. These effects, particularly projection for SZ and optical signatures, deserve further exploration (Noh & Cohn 2012; White, Cohn & Smit 2010; Angulo et al. 2012).

## 5 SUMMARY

Using polynomial log-space approximations to the high-mass end of the cosmic mass function, we present analytic forms for statistics of multi-observable properties of the high-mass halos that host groups and clusters of galaxies. The model employs scaling laws between observables and mass that are power-law in the mean with log-normal covariance.

The model provides quick estimation of cluster counts as a function of multiple observables and calculation of conditional likelihoods for observable-selected samples, both of which are directly relevant for joint survey analysis or follow-up observations. By comparing to a locally-convolved Tinker mass function, we show that the first-order model is generally accurate within a narrow range near the pivot mass, except for very high mass-scatter proxies. The second and third-order extensions provide increasingly wider coverage in observables irrespective of the mass scatter. The third-order model is nearly global in scope.

The mass variance in a particular observable determines many expected features, as does the covariance between pairs of observables at fixed mass. As multi-wavelength surveys and dedicated follow-up campaigns provide increasingly rich, uniform samples of clusters, opportunities to apply this model to better constrain the statistical properties of massive halos will become apparent. Such knowledge will provide useful constraints on the physical processes that govern baryon evolution in massive halos.

**ACKNOWLEDGMENTS**

We thank the organizers of the “Monsters Inc.” workshop on clusters at KITP, supported in part by the National Science Foundation under Grant No. PHY05-51164, where this work initiated. We thank Eduardo Rozo and Jim Bartlett for useful suggestions. The mass function calculations were obtained from <http://hmf.icrar.org/> using source code developed by Steven Murray and collaborators at <http://github.com/steven-murray/hmf/>. AEE acknowledges NASA NNX07AN58G and the Mairie de Paris “Research in Paris” program for support, and thanks Gary Mamon and Joe Silk for sabbatical hosting assistance at IAP. PA thanks A. Milliken and the Michigan Center for Theoretical Physics for hospitality and acknowledges support from the French Fonds de Solidarité et de Développement des Initiatives Étudiantes (FSDIE).

**APPENDIX A: THIRD-ORDER MODEL****A1 Multi-property halo number density**

The accuracy gained in going from  $n_1(s)$  to  $n_2(s)$  motivates a third-order approach. We thus now consider

$$n_3(\mu) = Ae^{-\beta_1\mu - \frac{1}{2}\beta_2\mu^2 - \frac{1}{6}\beta_3\mu^3}, \quad (\text{A1})$$

where  $\beta_3 = -[(d^3/d\mu^3) \ln n_{\text{exact}}](\mu=0) > 0$ . We could not find a closed form solution at this order, so we instead consider the approximation that limits the mass range to be near enough to the pivot point so that

$$n_3(\mu) \simeq n_2(\mu) \left(1 - \frac{1}{6}\beta_3\mu^3\right). \quad (\text{A2})$$

Convolving this approximated form of  $n_3(\mu)$  with  $P(\mathbf{s}|\mu)$  yields

$$n_3(\mathbf{s}) = n_2(\mathbf{s}) \left\{1 - \frac{\beta_3}{2} \left(\sigma_{\mu|\mathbf{s},2}^2 \langle \mu|\mathbf{s} \rangle_2 + \frac{1}{3} \langle \mu|\mathbf{s} \rangle_3^2\right)\right\}. \quad (\text{A3})$$

One can see clearly that the signal range will be limited from above by the requirement that the space density be non-negative.

**A2 Selecting on an observable property**

We have  $P_3(s_b|s_a) = n_3(s_a, s_b)/n_3(s_a)$ , which, using the previous formula, gives

$$P_3(s_b|s_a) = P_2(s_b|s_a) \times \frac{1 - \frac{\beta_3}{2} (\sigma_{\mu|a,b,2}^2 \langle \mu|s_a, s_b \rangle_2 + \frac{1}{3} \langle \mu|s_a, s_b \rangle_3^2)}{1 - \frac{\beta_3}{2} (\sigma_{\mu|a,2}^2 \langle \mu|s_a \rangle_2 + \frac{1}{3} \langle \mu|s_a \rangle_3^2)}. \quad (\text{A4})$$

We can calculate analytically the mean and variance of  $P_3(s_b|s_a)$ , which gives

$$\langle s_b|s_a \rangle_3 = K_1 J_1 - K_2 C (J_2 + D J_1) - K_3 C^3 (J_4 + 3D J_3 + 3D^2 J_2 + D^3 J_1) \quad (\text{A5})$$

$$\sigma_{b|a,3}^2 = K_1 J_2 - K_2 C (J_3 + D J_2) - K_3 C^3 (J_5 + 3D J_4 + 3D^2 J_3 + D^3 J_2) - \langle s_b|s_a \rangle_3^2, \quad (\text{A6})$$

where

$$J_n = \int_{-\infty}^{+\infty} s_b^n P_2(s_b|s_a) ds_b \quad (\text{A7})$$

$$= \frac{1}{\sqrt{\pi}} \sum_{k=0}^{\lfloor n/2 \rfloor} \binom{n}{2k} M^{n-2k} (2\sigma^2)^k \Gamma(k+1/2) \quad (\text{A8})$$

$$M = \langle s_b|s_a \rangle_2 \quad (\text{A9})$$

$$\sigma = \sigma_{b|a,2} \quad (\text{A10})$$

(In particular :  $J_0 = 1$ ,  $J_1 = M$ ,  $J_2 = \sigma^2 + M^2$ ) and

$$C = \frac{X \sigma_{(\mu|a,b),1}}{1 - r_{ab}^2} \quad (\text{A11})$$

$$D = \frac{1}{X} [Y - X\pi_b - \beta_1(1 - r_{ab}^2)] \quad (\text{A12})$$

$$X = \frac{\alpha_b}{\sigma_b^2} - \frac{r_{ab}\alpha_a}{\sigma_a\sigma_b} \quad (\text{A13})$$

$$Y = (s_a - \pi_a) \left( \frac{\alpha_a}{\sigma_a^2} - \frac{r_{ab}\alpha_b}{\sigma_a\sigma_b} \right) \quad (\text{A14})$$

$$K_1 = \left[ 1 - \frac{\beta_3}{2} \left( \sigma_{\mu|\mathbf{s},2}^2 \langle \mu|\mathbf{s} \rangle_2 + \frac{1}{3} \langle \mu|\mathbf{s} \rangle_3^2 \right) \right]^{-1} \quad (\text{A15})$$

$$K_2 = K_1 \frac{\beta_3}{2} \sigma_{(\mu|a,b),1} x_{a,b}^2 \quad (\text{A16})$$

$$K_3 = K_1 \frac{\beta_3}{6} x_{a,b}^3. \quad (\text{A17})$$

**References**

- Allen S. W., Evrard A. E., Mantz A. B., 2011, *Ann. Rev. Astron. Astrophys.*, 49, 409  
 Andreon S., Hurn M. A., 2010, *MNRAS*, 404, 1922  
 Angulo R. E., Springel V., White S. D. M., Jenkins A., Baugh C. M., Frenk C. S., 2012, *MNRAS*, 426, 2046  
 Arnaud M., Pointecouteau E., Pratt G. W., 2005, *A&A*, 441, 893  
 Balaguera-Antolínez A., Sánchez A. G., Böhringer H., Collins C., 2012, *MNRAS*, 425, 2244  
 Battaglia N., Bond J. R., Frommer C., Sievers J. L., 2013, *ApJ*, 777, 123  
 Benson B. A. et al., 2013, *ApJ*, 763, 147  
 Bhattacharya S., Heitmann K., White M., Lukić Z., Wagner C., Habib S., 2011, *ApJ*, 732, 122  
 Biffi V., Sembolini F., De Petris M., Valdarnini R., Yepes G., Gottlöber S., 2014, *MNRAS*  
 Böhringer H., Dolag K., Chon G., 2012, *A&A*, 539, A120  
 Cui W., Borgani S., Murante G., 2014, *ArXiv e-prints*  
 Cusworth S. J., Kay S. T., Battye R. A., Thomas P. A., 2013, *ArXiv e-prints*  
 Ettori S., 2013, *MNRAS*, 435, 1265  
 Evrard A. E. et al., 2008, *ApJ*, 672, 122  
 Evrard A. E. et al., 2002, *ApJ*, 573, 7  
 Fabjan D., Borgani S., Rasia E., Bonafede A., Dolag K., Murante G., Tornatore L., 2011, *MNRAS*, 416, 801

- Giodini S., Lovisari L., Pointecouteau E., Ettori S., Reiprich T. H., Hoekstra H., 2013, *Space Science Reviews*, 177, 247
- Henry J. P., Evrard A. E., Hoekstra H., Babul A., Mahdavi A., 2009, *ApJ*, 691, 1307
- Israel H., Reiprich T. H., Erben T., Massey R. J., Sarazin C. L., Schneider P., Vikhlinin A., 2014, *ArXiv e-prints*
- Jenkins A., Frenk C. S., White S. D. M., Colberg J. M., Cole S., Evrard A. E., Couchman H. M. P., Yoshida N., 2001, *MNRAS*, 321, 372
- Jiang L., Helly J. C., Cole S., Frenk C. S., 2013, *ArXiv e-prints*
- Koester B. P. et al., 2007, *ApJ*, 660, 239
- Le Brun A. M. C., McCarthy I. G., Schaye J., Ponman T. J., 2013, *ArXiv e-prints*
- Mantz A., Allen S. W., Rapetti D., Ebeling H., 2010, *MNRAS*, 406, 1759
- Martizzi D., Mohammed I., Teyssier R., Moore B., 2013, *ArXiv e-prints*
- Maughan B. J., 2007, *ApJ*, 668, 772
- Maughan B. J., 2014, *MNRAS*, 437, 1171
- Mortonson M. J., Hu W., Huterer D., 2011, *Phys. Rev. D*, 023015
- Munari E., Biviano A., Borgani S., Murante G., Fabjan D., 2013, *MNRAS*, 430, 2638
- Murray S. G., Power C., Robotham A. S. G., 2013, *Astronomy and Computing*, 3, 23
- Nelson K., Lau E. T., Nagai D., Rudd D. H., Yu L., 2014, *ApJ*, 782, 107
- Noh Y., Cohn J. D., 2012, *MNRAS*, 426, 1829
- Planck Collaboration, 2011, *ArXiv e-prints*: 1101.2027
- Planck Collaboration et al., 2013, *ArXiv e-prints*
- Pratt G. W., Croston J. H., Arnaud M., Böhringer H., 2009, *A&A*, 498, 361
- Rasia E. et al., 2012, *New Journal of Physics*, 14, 055018
- Rozo E., Bartlett J. G., Evrard A. E., Rykoff E. S., 2014c, *MNRAS*, 438, 78
- Rozo E., Evrard A. E., Rykoff E. S., Bartlett J. G., 2014b, *MNRAS*, 438, 62
- Rozo E., Rykoff E. S., 2013, *ArXiv e-prints*
- Rozo E., Rykoff E. S., Bartlett J. G., Evrard A., 2014a, *MNRAS*, 438, 49
- Rozo E., et al., 2010, *ApJ*, 708, 645
- Ruel J. et al., 2013, *ArXiv e-prints*
- Rykoff E. S. et al., 2012, *ApJ*, 746, 178
- Rykoff E. S. et al., 2008, *ApJ*, 675, 1106
- Rykoff E. S. et al., 2013, *ArXiv e-prints*
- Saliwanchik B. R. et al., 2013, *ArXiv e-prints*
- Sheth R. K., Mo H. J., Tormen G., 2001, *MNRAS*, 323, 1
- Sievers J. L. et al., 2013, *JCAP*, 10, 60
- Stanek R., Rasia E., Evrard A. E., Pearce F., Gazzola L., 2010, *ApJ*, 715, 1508
- Stanek R., Rudd D., Evrard A. E., 2009, *MNRAS*, 394, L11
- Tinker J., Kravtsov A. V., Klypin A., Abazajian K., Warren M., Yepes G., Gottlöber S., Holz D. E., 2008, *ApJ*, 688, 709
- Vikhlinin A. et al., 2009, *ApJ*, 692, 1033
- Voit G. M., 2005, *Reviews of Modern Physics*, 77, 207
- von der Linden A. et al., 2014, *ArXiv e-prints*
- Weinberg D. H., Mortonson M. J., Eisenstein D. J., Hirata C., Riess A. G., Rozo E., 2013, *Physics Reports*, 530, 87
- White M., Cohn J. D., Smit R., 2010, *MNRAS*, 408, 1818
- Zhang Y.-Y., Andernach H., Caretta C. A., Reiprich T. H., Böhringer H., Puchwein E., Sijacki D., Girardi M., 2011, *A&A*, 526, A105